

Current-driven nonequilibrium electrodynamics in graphene revealed by nano-infrared imaging

Received: 1 August 2024

Accepted: 8 April 2025

Published online: 24 April 2025

Check for updates

Y. Dong^{1,2}✉, Z. Sun², I. Y. Phinney^{3,4}, D. Sun², T. I. Andersen⁴, L. Xiong², Y. Shao^{2,8}, S. Zhang², Andrey Rikhter⁵, S. Liu⁶, P. Jarillo-Herrero³, P. Kim⁴, C. R. Dean², A. J. Millis², M. M. Fogler⁵, D. A. Bandurin⁷✉ & D. N. Basov²✉

Electrons in low-dimensional materials driven out of equilibrium by a strong electric field exhibit intriguing effects that have direct analogues in high-energy physics. In this work we demonstrate that two of these effects can be observed in graphene, leading to relevant implications for light-matter interactions at the nanoscale. For doped graphene, the Cherenkov emission of phonons caused by the fast flow of out-of-equilibrium electrons was found to induce direction-dependent asymmetric plasmon damping and an unexpected generation of photocurrent. For graphene close to charge neutrality, incident infrared photons were found to disrupt the creation-recombination balance of electron-hole pairs enabled by the condensed matter version of the Schwinger effect, resulting in an excess photocurrent that we term Schwinger photocurrent. Both Schwinger and Cherenkov photocurrents are different from other known light-to-current down conversions scenarios and thus expand the family of photoelectric effects in solid state devices. Through nano-infrared imaging methodology, we provide a more comprehensive view of current-driven nonequilibrium electrodynamics in graphene.

A strong electromagnetic field can drive quantum materials out of equilibrium, such as by pulsed light fields and by high electric biases. The former has been intensively studied for graphene with many interesting phenomena such as the Floquet effect¹, light-induced anomalous Hall effect², and plasmon switching³. These effects typically appear in (sub-)picosecond timescales and are challenging to capture by static observables. High-current-driven nonequilibrium^{4–14}, on the other hand, leads to quasi-steady-state observables spanning across a broad range of energy scales (Fig. 1). In DC transport, two prominent causes of nonlinear electrical responses are phonon drag¹⁵ and Schwinger pair generation^{6–11}. The former leads to reduced

conductivity and increased thermal power by electron-phonon interaction. The latter Schwinger effect, originally proposed in quantum electrodynamics⁹ as particle-antiparticle pair creation in vacuum by strong electric fields, has later been emulated in graphene^{6–8,10,11}. Moving beyond DC responses, nonequilibrium acoustic waves emission^{4,12–14} covers frequencies from gigahertz (GHz)⁴ to terahertz (THz)¹² when the speed of phonons is surpassed by the drifting carriers. The phenomenon is called Cherenkov phonon emission because the speed criteria for electrons and phonons resembles a Cherenkov cone^{13,14}. Beyond lattice vibrations, the behaviors of collective electronic oscillations—known as plasmons, which span nearly the entire

¹Department of Applied Physics and Applied Mathematics, Columbia University, New York, NY, USA. ²Department of Physics, Columbia University, New York, NY, USA. ³Department of Physics, Massachusetts Institute of Technology, Cambridge, MA, USA. ⁴Department of Physics, Harvard University, Cambridge, MA, USA. ⁵Department of Physics, University of California San Diego, La Jolla, CA, USA. ⁶Department of Mechanical Engineering, Columbia University, New York, NY, USA. ⁷Department of Materials Science and Engineering, National University of Singapore, Singapore, Singapore. ⁸Present address: Department of Physics, Pennsylvania State University, University Park, PA, USA. ✉e-mail: yd2400@columbia.edu; dab@nus.edu.sg; db3056@columbia.edu

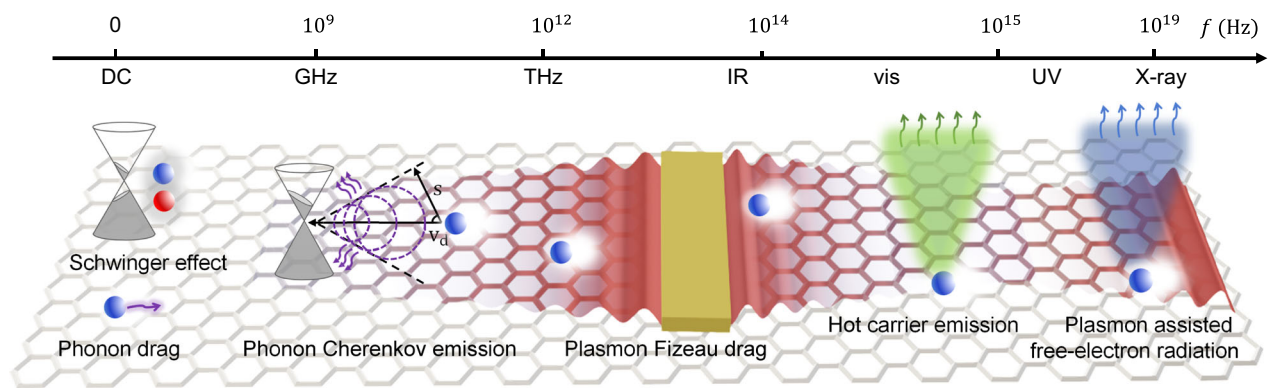


Fig. 1 | Energy spectrum of responses in high current driven graphene. For DC conductivity, the Schwinger mechanism^{6–11} and phonon drag¹⁵ would introduce nonlinear transport behaviors. From GHz to THz range, acoustic wave emission can be induced by Cherenkov-like electron-phonon instability^{4,12–14} when carrier drift velocities exceed the speed of sound. Observed in mid-infrared (MIR) and

extendable to other range, the plasmon Fizeau drag^{16,17} refers to the effect that plasmon dispersion diverges in different directions when subjected to electric current. These plasmons are also predicted to assist visible¹⁸ to X-ray radiation¹⁹ through interactions with hot carriers. To date, only the hot carrier emission has already been observed^{20,21} in visible and near-infrared (NIR) range.

spectrum from DC to UV—are also significantly altered by high currents. Fizeau drag^{16,17} has been experimentally identified in mid-infrared range which breaks optical nonreciprocity by current flow. Moreover, considering plasmons to interact with hot electrons of very high kinetic energies, it has been predicted that quantum Cherenkov effect for plasmonic emission could occur for near-infrared (NIR) to visible range¹⁸ with even ultraviolet (UV) to X-ray range imitating free-electron lasers¹⁹ possible. While these two predictions are yet to be experimentally realized, it has been observed that hot carriers in graphene generate electroluminescence²⁰ and thermal emission²¹ visible to human eyes. The diverse AC responses of current-driven graphene depicted in Fig. 1 herald the necessity of studying current-driven nonequilibrium in the framework of light-matter interaction.

In this study, we employ cryogenic nano-infrared imaging techniques to uncover the local behaviors of current-driven nonequilibrium in graphene. The plasmon polariton scattering rate acts as a sensitive probe to local acoustic phonons in highly doped graphene. Moreover, the observed nano-photocurrents under different conditions reveal insights into Cherenkov phonon emission and Schwinger carrier generation.

Results

Nano-infrared imaging methodology

We used a hybrid of nano-infrared imaging modalities including scanning near-field optical microscopy (SNOM) and photocurrent nanoscopy^{22–25} to reveal the nonequilibrium electrodynamics in graphene. The former modality collects nearfield optical scattering signals while the latter method collects current signals, both of which assisted by local demodulation from tapping-mode atomic force microscopy (AFM), with more details in Methods. As illustrated in Fig. 2a, mid-infrared (MIR) laser beam of $\omega = 890 \text{ cm}^{-1}$ was focused on the devices where gold electrodes served as both electrical ground and plasmons launchers. We selected this laser energy at MIR because it provided an optimal range for imaging plasmons, which served as key indicators of the electrodynamics in graphene. However, these phenomena are universal and also influence photoconductivity responses across other energy ranges. The hBN-encapsulated graphene devices were shaped into ribbons of $2 \mu\text{m}$ width and assembled on silicon or graphite gates (Methods). The metallic tip both enhanced the local electromagnetic field (red Gaussian profile in Fig. 2a) and provided additional local gating (Supplementary Notes 2). The photocurrent responses are collected non-locally by contacts which can be understood by Shockley-Ramo mechanism²⁶. In both nano-

infrared imaging modalities above, the spatial resolution was mainly determined by the diameter of the AFM tip apex around 15 nm. The multi-messenger nano-infrared imaging methodology bridges the electronic and optical observables to probe light-matter interactions at the nanoscale. As listed at the top left of Fig. 2a, infrared plasmon polaritons possess a phase velocity ($\sim 10^5 \text{ m/s}$) which is between velocities of acoustic phonons ($\sim 10^4 \text{ m/s}$) and Fermi velocity of electrons ($\sim 10^6 \text{ m/s}$) in graphene. Therefore, there are anticipated interplays among these quasi-particles under high current biases to be probed by nano-infrared imaging.

The schematic device in Fig. 2a demonstrates the single ribbon area where nano-infrared imaging experiments were conducted. It corresponds to the black dashed rectangles in Fig. 2b, c. Figure 2b, c present SNOM and nano-photocurrent scans of a typical graphene device, collected at $T = 170 \text{ K}$ in the absence of gate and current biases. When the device is charge-neutral, there would be no plasmon fringes in the nano-infrared images and the nano-photocurrent signals primarily arise at the boundaries between the graphene and gold, or charge puddles due to Seebeck effect^{22–25,27,28} as shown in Fig. 2b, c. When the device is doped by applying back-gate voltages, plasmons would appear and photocurrent signals would also be altered by DC current as demonstrated in later sections.

Before presenting the experimental results in detail, we provide a summary of the observables and their connections to the claimed current-driven nonequilibrium effects. In highly doped graphene, we studied two distinct observables related to the Cherenkov phonon emission effect: infrared plasmonic fringes and nano-photocurrent. First, we observed asymmetric damping of plasmons with respect to the current direction in both gate polarities. This asymmetry was linked to the Cherenkov emission of acoustic phonons^{4,12–14} (Section Asymmetric plasmon damping with Cherenkov phonons). Second, we observed nano-photocurrents with spatial, current, and gate dependencies that surpassed the expectations of conventional photothermoelectric (PTE)^{22–25,27,28} and bolometric^{29,30} mechanisms. Notably, the nano-photocurrents exhibited a regime with reversed sign at high current densities. The deviation was explained using a tip-gating-influenced Cherenkov phonon emission model (Section Nano-photocurrent with Cherenkov phonons). Finally, in graphene near the charge neutrality point (CNP), we detected nano-photocurrent signals featuring prominent peaks (dips) whose behaviors could not be explained by equilibrium mechanisms. Mixed with Seebeck contribution, the Schwinger mechanism coupled with self-gating led to the observed photocurrent peaks (dips) at the CNP, where excess

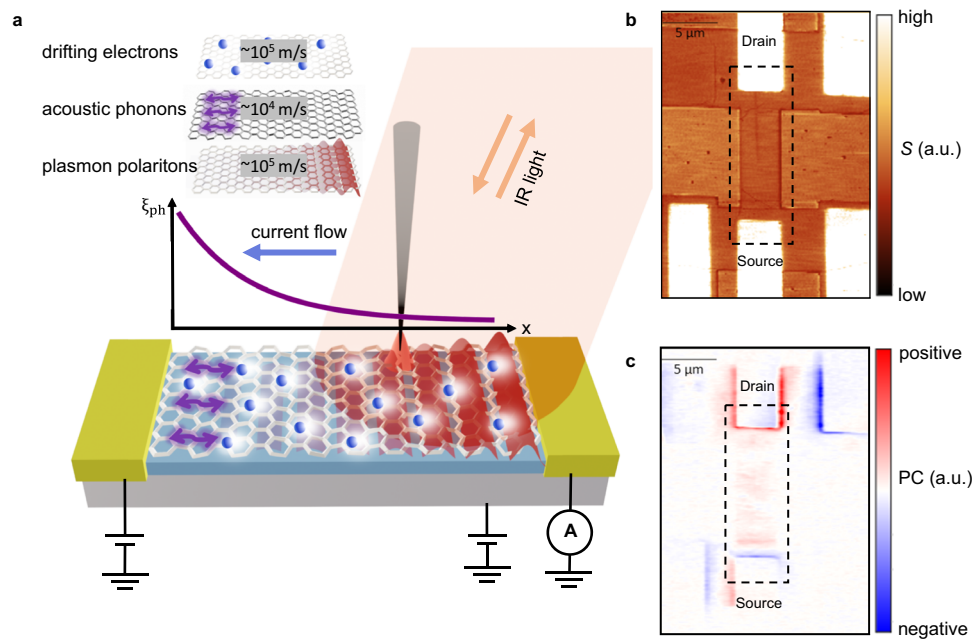


Fig. 2 | Experimental setup for visualizing electron-phonon dynamics of graphene. **a** Schematic of a representative device. The hBN (hexagonal boron nitride) encapsulated graphene device was assembled on tunable back gate with patterned gold contacts. When the device was illuminated with infrared light, gold electrodes launched graphene plasmons. Cartoons of drifting electrons, acoustic phonons and plasmon polaritons are presented as shadowed moving blue balls, wiggled purple arrows and red fringes, respectively; we also indicate the magnitude of their group

velocities in inset. Under the DC current, the nonequilibrium acoustic phonons would grow along the current flow (x-axis) in exponential manner with population ξ_{ph} illustrated by a purple curve. **b**, **c** SNOM (scanning nearfield optical microscopy) and nano-photocurrent images of a typical device at zero back gate and zero current. The nearfield scattered optical signals (S) and photocurrent signals (PC) were plotted in arbitrary units. The black-dashed framed regions are main area of study as displayed in (a).

photocarriers were generated by the strong lateral fields (Section Nano-photocurrent with Schwinger effect).

Asymmetric plasmon damping with Cherenkov phonons

Drifting electrons with supersonic velocities can stimulate phonon emission with exponential growth of their population, known as phonon Cherenkov amplification, or electron-phonon instability^{4,12–14}. In this section we endeavor to explore the behavior of plasmons in the regime where the Cherenkov emission is expected and found systematic asymmetric plasmon damping as elaborated below. Figure 3a, b demonstrate the real-space images of propagating plasmons launched at drain contact with different DC biases, separately for electron and hole doping. Similar to other nearfield imaging experiments^{16,17,31}, the propagating graphene plasmons manifests themselves as oscillating fringes with periods of plasmon wavelength as a function of tip position. By scanning in the middle of the graphene device (Fig. 2) and varying the DC current, we captured the current dependence of plasmon propagation at $T = 170$ K. In Fig. 3a, b, the x- and y-axes denote the values of the DC current and the scanner position, respectively. The gray dashed lines mark the zero current data while the white dotted lines suggest plasmon propagation ranges. Directions of carrier flow and plasmon propagation are indicated as straight and wavy arrows, separately. The propagation ranges of plasmons were found to be altered at extremely high current densities ($>10^3$ A/m) and quite different when they were counter-propagating versus co-propagating with the carrier flow. In the hole-doped regime (Fig. 3a), when carriers and plasmons were co-propagating (negative current), a milder reduction of plasmon propagation range was observed than counter-propagating (positive current). On the other hand, in the electron-doped regime (Fig. 3b), there was a stronger reduction of the plasmon propagation range with negative current which was also the counter-propagation. The entirety of observations at different gate and current polarities reveals more prominent plasmon damping

for plasmons propagating against the carrier flow and phonon emission.

To better understand the plasmonic behavior of graphene under current-driven nonequilibrium, we extract the plasmon quality (Q) factors³¹ defined via complex momentum $q = q_1 + iq_2$ as $Q = \frac{q_1}{q_2}$. By fitting 15 evenly spaced lines acquired at different current biases in Fig. 3a, we obtained the current dependence of Q factors (Fig. 3c). At current biases exceeding around 1 mA, we observed a sudden drop in Q factor that was stronger for plasmons counter-propagating with the electronic flow. Electronic heating was inevitable in high-current experiments but could not lead to the Q factor asymmetry. Searching for direction-dependent mechanisms of Q factor reduction, we considered thermoelectric effects such as Peltier and Thomson effect. However, these effects could only change the electron temperature by a few Kelvins^{32–34}, which could not alter plasmon quality factor visibly³⁰ under the conditions of this experiment. Therefore, we attribute the asymmetric plasmon damping to nonequilibrium phonons as detailed below.

The plasmonic wavevector in high-mobility graphene can be used to extract the electronic conductivity of graphene at the frequency of infrared imaging experiments as: $\sigma = \sigma_1 + i\sigma_2 = \frac{i\kappa\omega}{2\pi q}$ where κ is the effective dielectric function of environment of graphene layer, ω is frequency and q is the plasmon wave vector. Accordingly, the reciprocal of the quality factor $Q^{-1} = \frac{q_2}{q_1} \approx \frac{\sigma_1}{\sigma_2} + \frac{\kappa_2}{\kappa_1}$ can be partitioned into two terms representing dissipation (damping) in the graphene channel ($\frac{\sigma_1}{\sigma_2}$) and effective dielectric losses ($\frac{\kappa_2}{\kappa_1}$). Driving the system out of equilibrium, both optical³⁵ and acoustic phonon^{4,12–14} scattering can be drastically enhanced. The quantities presented in Fig. 3d were calculated by making comparisons with ref. 31 and assuming that the additional dissipation observed in the counter-propagating regime stems from the emission of acoustic phonons. This assumption is justified by the following momentum and energy conservation criteria in addition to the speed criterion ($v_d > s$, s is the speed of phonons) for

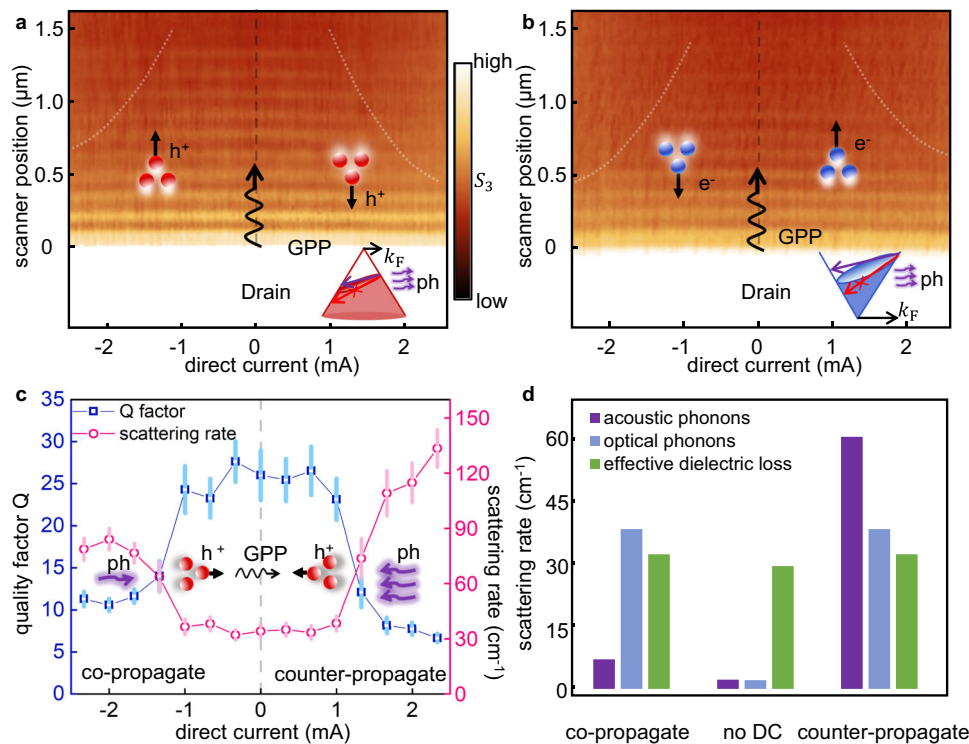


Fig. 3 | Asymmetric damping of graphene plasmon polaritons (GPP). Real-space propagation (y-axis) of plasmons imaged by scanning near-field optical microscope under different current flow (x-axis) with carrier densities $p = +3.3 \times 10^{12} \text{ cm}^{-2}$ for (a) and $n = -2.3 \times 10^{12} \text{ cm}^{-2}$ for (b). **a, b** share the same color bar, and the third order pseudo-heterodyne signals (S_3) were plotted for nearfield imaging of plasmons. The imaging data at varied DC current were taken at the same position in the middle of graphene device. The dashed gray line marks the zero-bias data of propagating plasmons and the white dotted curves sketch propagating length of plasmons. The cartoons of moving carriers with arrows indicate the different velocity directions of electrons and holes. The propagating plasmons are labeled as wiggled arrows launched from the bright gold launcher at the bottom. The Dirac cone animations at bottom right of (a, b) indicate the momentum and energy criteria for phonon

emission. The purple direct arrows represent that the allowed phonon momentum gained from drifting electrons is smaller than $2k_F$ (k_F , Fermi momentum). The red arrows demonstrate that phonons of energy larger than $2\hbar k_F v_d$ are prohibited to emit (v_d , carrier drift velocity). **c** Quality factors and scattering rates of propagating plasmons under different direct current biases. Scattering rates are derived from quality factors by dividing by the excitation frequency. Quality factors are extracted by fitting plasmon waves^{16,17,31} with standard errors presented as bars. **d** Histograms illustrating the contributions from various scattering channels are shown for regimes where plasmons counter-propagate or co-propagate with the carrier flow at the maximum currents in (c), and in the absence of DC flow. These values are determined by comparison with ref. 31, with further details provided in Supplemental Notes 1.

Cherenkov phonons^{4,12–14}. Considering the Dirac band structure of graphene, momentum and energy conservation laws limit the phonon branches that can emit by gaining momentum and energy from drifting electrons. As shown in the insets of Fig. 3a, b, the maximum momentum transferred from electrons to phonons is smaller than twice of Fermi momentum (purple arrows); and the maximum energy smaller than the energy difference between the highest and lowest levels of the tilted Fermi surface (red arrows are prohibited). Therefore, the Cherenkov phonon emission only applies to the acoustic phonons in graphene, which accumulate along the flow and thus scattered with plasmons more heavily at the downstream. The asymmetric plasmonic damping by Cherenkov phonons occurs across a wide temperature range. The influence of Cherenkov phonons on scattering rate would become more pronounced at lower temperatures¹², where the intrinsic plasmon quality factor is also higher³¹. The graphene optical phonons³⁴, on the other hand, were symmetrically enhanced with different directions due to electron heating. They were prohibited from Cherenkov emission because of the energy mismatch ($\gg 2\hbar k_F v_d$) (red arrows in inset of Fig. 3a, b). It is worth mentioning that hyperbolic optical phonon polaritons in the adjacent hBN layers could also be driven to emit^{36,37}. This emission could potentially scatter with plasmons³⁸ leading to additional symmetric damping. In a nutshell, the current-driven nonequilibrium acoustic phonons that distribute unevenly across sample scattered with plasmons and resulted in an asymmetric damping effect.

Nano-photocurrent with Cherenkov phonons

Photocurrent²⁴ nanoscopy is sensitive to both optical and electronic properties of graphene and ideal to reveal light-matter interaction. In this section, we examined the consequences from Cherenkov phonon instability in nano-photocurrent signals. Conventionally, unbiased graphene photocurrent is dominated by PTE mechanism^{22–25,27,28} while unbiased graphene photocurrent is dominated by bolometric effect^{29,30} (Supplemental Table 1, Supplemental Notes 3–4), which we have observed for equilibrium regime. Similar to the presentation of nano-optical signals in Fig. 3a, b, the nano-photocurrent data in Fig. 4a, b were taken by repeatedly scanning in the middle of the graphene device while varying the DC current flow. The intensity of the color maps represented the magnitudes of the second-order tip-modulated nano-photocurrent signals. The sign was appointed as positive (red) from source to drain. The device was gated into $p = 3.3 \times 10^{12} \text{ cm}^{-2}$ (Fig. 4a) and $n = -4.4 \times 10^{12} \text{ cm}^{-2}$ (Fig. 4b) for comparison of different carrier types. Line profiles taken at different locations in Fig. 4b were then displayed in Fig. 4c for detailed examination. At zero current, there were only photocurrent signals at the interface of graphene and gold (marked by black arrows in Fig. 4c) attributable to Seebeck effect^{22–25,27,28}. As DC bias was applied, the photocurrent signals were markedly enhanced by bolometric effect^{29,30} enabling imaging of plasmon fringes. Since the bolometric photocurrent in biased graphene has only been revealed in far field experiment³⁰ to date, here we briefly clarify the bolometric mechanism

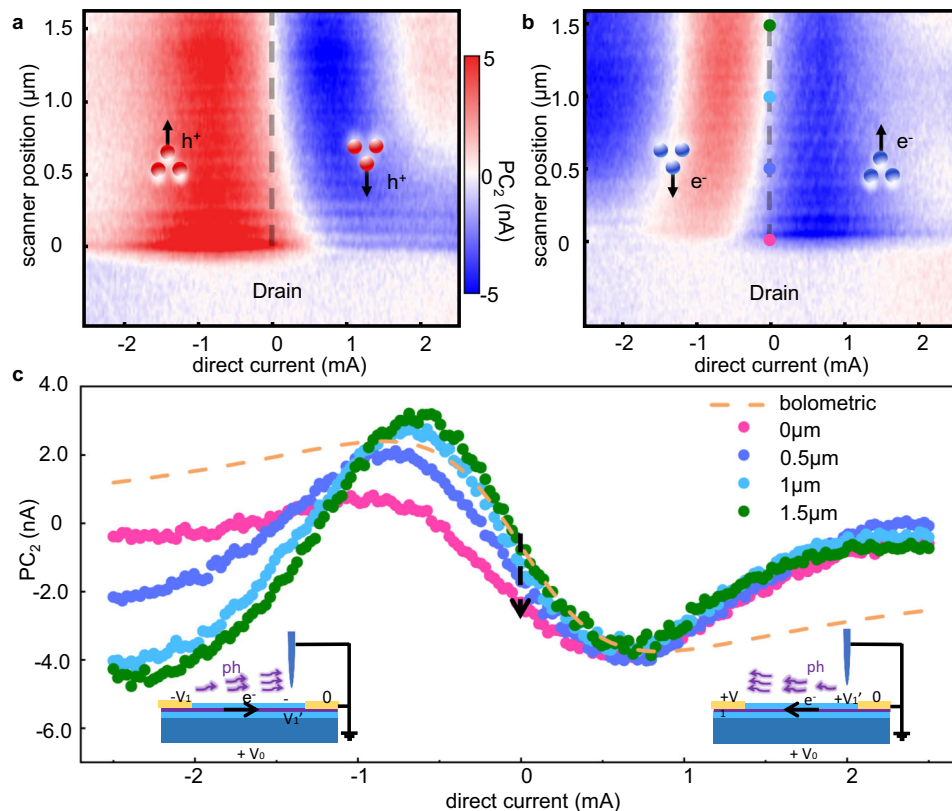


Fig. 4 | Nano-photocurrent with Cherenkov phonons. Second-order demodulated nano-photocurrents (PC_2) were taken under different DC current scanned along the same middle line of the graphene device with carrier densities $p = 3.3 \times 10^{12} \text{ cm}^{-2}$ for (a) and $n = -4.4 \times 10^{12} \text{ cm}^{-2}$ for (b). Similar to the presentation of Fig. 3a, b the y-axes indicate the scanning positions and cartoons of carriers indicated the flow directions. The vertical dashed gray line marks the zero-bias data. The cartoons of moving carriers with arrows indicate the different velocity directions of electrons and holes. a, b share the same color bar. The four colored dots in the middle of (b) marked the positions where data in (c) were taken. c DC

current dependent nano-photocurrent line profiles taken from different positions in (b). The dashed orange curve represents anticipated bolometric photocurrent extracted from the simultaneously taken transport experiment. The black dashed arrow marks the amount of PTE (photo-thermoelectric) current without current bias. The insets demonstrated the corresponding scenarios of effective tip-gating effect, where V_0 , V_1 and V_1' represents backgate voltage, bias voltage and local potential of graphene. Light blue, purple and dark blue represent hBN, graphene, and additional gate dielectric layers of the sample stacks. Purple arrows animate the Cherenkov phonon emission.

in nano-photocurrent. Bolometric effect²⁹ refers to the fact that heating would increase the resistivity of the material. As the tapping AFM tip scans along the sample, it enhances and demodulates the local electromagnetic field (δE_{AC}), as well as its second order effect (δE_{AC}^2) which is proportional to the heating and bolometric photocurrent. Therefore, when sample is biased by E_{DC} , it is a third-order conductivity³⁹ term, $\sigma^{(3)} E_{DC} \delta E_{AC}^2$, that is responsible for generating the bolometric nano-photocurrent. With the nano-photocurrent formalism that we established in the Supplemental Notes 3–4, the local bolometric photocurrent across a current-carrying device can be expressed by $\delta I_{Bol} = -I \frac{\partial R}{R(I) + T \partial R} \int_0^1 dx \delta T(x)$, where R , T , I represents the resistance, temperature and current, respectively; 0 and 1 stands for the left and right ends of the device. This equation produced the orange dashed curve in Fig. 4, based on the simultaneously measured nonlinear I–V relation. Combined with the additional Seebeck contribution at zero bias (indicated by the arrow in Fig. 4c), the nano-photocurrent under small DC current densities can be well understood.

Surprisingly, as current densities increased to milliamper level, the photocurrents diverged from the equilibrium photocurrent behaviors. The photocurrent curves in Fig. 4c were first suppressed compared with bolometric trends and then reversed the direction, especially with negative biases. For both carrier types (Fig. 4a, b), the configuration where nano-photocurrent switched sign coincided with the conditions where plasmon damped faster by the electron-phonon instability in previous section. We attribute this new regime of

photocurrents to Cherenkov phonon emission, which exhibits distinct current and gate polarity dependences (Supplemental Table 1) compared to the Seebeck and bolometric regimes. Additional data mapped in a full device shape can be found in Supplemental Notes 7, where a gradual photocurrent sign-reversal behavior was observed across the device.

To understand the tip perturbed Cherenkov phonon emission in nano-photocurrent, we first revisit the Cherenkov phonon emission without a tip: electrons experience ‘friction’ and transfer momentum to the generated acoustic phonons, resulting in an increased resistance. In the scenario involving an AFM tip, however, the tip above the top hBN forms a capacitor with graphene (Supplemental Notes 2) and perturbs the local doping. For a biased device, the tip-graphene potential difference is zero at drain contact but nonzero away from it, with the latter case inducing local gate perturbation. The insets of Fig. 4c display the corresponding local gating scenarios for different current directions with V_0 , V_1 and V_1' denoting back gate voltage, bias voltage and local potential of graphene ($0 < V_1' < V_1$). As depicted in Supplemental Notes 2, for either gate polarity, the AFM tip could effectively increase the local doping level when it scanned near the drain electrode where more Cherenkov phonons were populated (Fig. 4c left inset). Since carrier density (n) was increased by the tapping tip (Supplemental Notes 2), the effective drift velocity $v_d = \frac{J_x}{ne}$ under tip was decreased, reducing Cherenkov phonon emission and the local resistance. Consequently, the tip-demodulated Cherenkov-phonon-induced signals were competing with the conventional

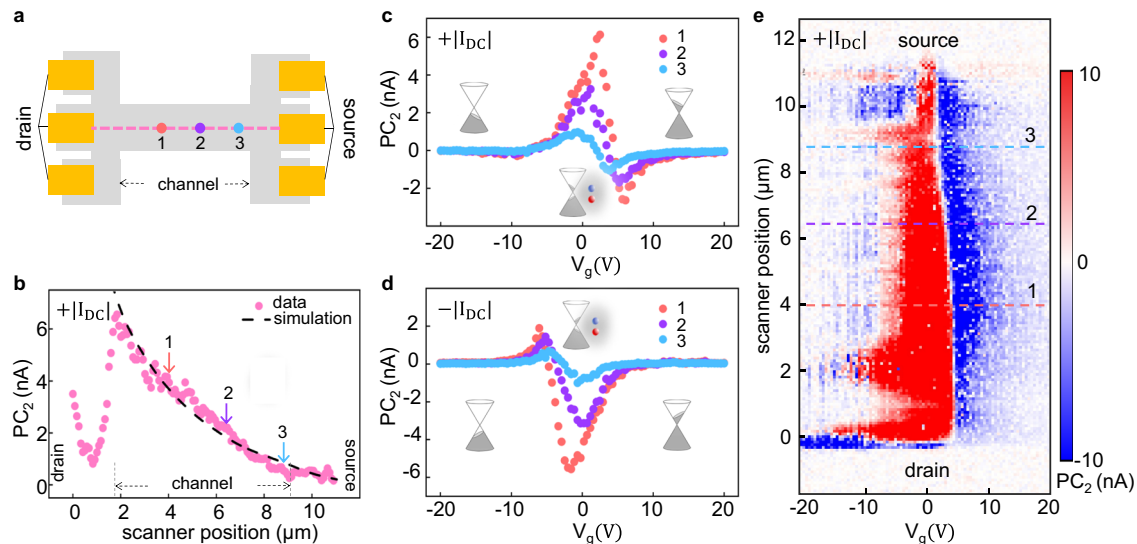


Fig. 5 | Schwinger effect in nano-photocurrent signals. **a** Illustration of the device shape. The gray part represents graphene with channel width $2\ \mu\text{m}$ and yellow parts represent gold electrodes. The pink dashed line indicates the location where data (**b**) was taken. The colored dots mark the positions 1–3 where data in (**c**, **d**) were taken. **b** Spatial dependent nano-photocurrent taken in the middle of the device with constant DC current $I_{\text{DC}} = +0.6\ \text{mA}$ applied. The pink dots are experimental data and the dashed line is simulation. The colored arrows

mark the positions 1–3 where data in (**c**, **d**) were taken. Back gate dependent nano-photocurrent at different positions 1–3 with constant DC current biases $I_{\text{DC}} = +0.6\ \text{mA}$ for **c** and $I_{\text{DC}} = -0.6\ \text{mA}$ for (**d**). The inset cartooned Dirac cones represent the different doping and Schwinger carrier generation regimes. **e** Color map of spatial and gate-dependent nano-photocurrent signals across the CNP, taken along the middle of device. The horizontal dashed lines mark the positions where data in (**c**) were taken.

bolometric photocurrent. This explains the discrepancy of experimental data in Fig. 4c from bolometric curve (orange dashed curve), with the difference correlated to Cherenkov phonon population and qualitatively conforms to the asymmetric plasmon damping in Fig. 3. The spatial dependence of the new photocurrent regime depicted by different colors in Fig. 4c (pink, purple, blue, green line profiles corresponding to 0, 0.5, 1, 1.5 μm to drain contact) can also be explained by the tip-induced local gating. The influence of tip on local gating was reduced as they approached the same electric potential, and so is the difference in the Cherenkov phonon induced photocurrent for two biasing polarities as shown by the pink curve in Fig. 4c. Therefore, the tip gating allowed us to reveal the Cherenkov phonons with nano-photocurrent observables.

Nano-photocurrent with Schwinger effect

In this section, we present that the Schwinger mechanism plays an important role in photocurrent generation in biased graphene close to CNP. To simplify the physics, the experiments were conducted at $T = 30\ \text{K}$, ensuring the system remained in the ballistic regime⁴⁰. As illustrated in Fig. 5a, we first recorded nano-photocurrents along the middle (dashed pink) line of the device to map the spatial distribution of the biased photocurrent with zero back-gate voltage (Fig. 5b). Biasing neutral graphene inevitably induces self-gating and spatial variations in both transverse (out-of-plane) and lateral electric fields, which can be calculated using a self-consistent method described in Supplemental Notes 6. We then positioned the probe at different locations (colored dots 1–3) while varying the global back-gate voltages and current polarities (Fig. 5c, d). Finally, the color map in Fig. 5e showed spatial and gate dependence collectively when the device was subjected to constant current.

The most prominent feature was an enhanced photoconductivity at CNP which manifested itself as nano-photocurrent signals with the same sign as DC biases (Fig. 5b–e). This observation disagreed with the bolometric photocurrents^{29,30} that should be opposite to DC biases. The spatial dependence of the signals at zero gate showed a monotonic increase from the source to the drain inside the graphene channel (Fig. 5b). Since the drain side experienced lower self-gating,

the observation of higher photocurrent signals with lower doping could not be explained by conventional photo-induced interband transition mechanism⁴¹ which positively correlated with doping. Interestingly, the observed spatial distribution aligned well with the Schwinger effect^{6–8,10,11} wherein intensive lateral fields break the “vacuum” at Dirac point generating electron-hole pairs that act as additional conductive carriers, akin to Landau-Zener-Klein interband tunneling³⁶. These Schwinger carriers could be activated by incident infrared photons and thus enhanced photoconductivity near the CNP. By solving the lateral field (E_x) distribution from the self-gating model (Supplemental Notes 6) and applying the relation $j_{\text{Schwinger}} \propto E_x^{\frac{3}{2}}$, we simulated the spatial distribution of Schwinger pairs (dashed black line in Fig. 5b), which captured the spatial dependence of the photocurrent peak at CNP.

To gain deeper insight into the photocurrent behavior, we examined its variation with back-gate voltages and current polarities at different positions, as shown in Fig. 5c, d. The pronounced peak (or dip) emerged around the CNP near the drain side (positions 1 and 2, orange and purple), alongside an antisymmetric-shape baseline near the source side (position 3, blue). While the antisymmetric contribution can be understood by Seebeck effect, the peak at the CNP requires the Schwinger-enabled photocurrent generation as shown in Fig. 5b. Comparing Fig. 5c, d, the central peak (dip) signals in data series 1 and 2 reversed sign for different current polarities, conforming to the expectation of Schwinger mechanism. In contrast, the antisymmetric shape for position 3 persisted because the parity from self-gating and Seebeck coefficient canceled each other (Supplemental Table 1). Therefore, while mixed with other effects, especially the Seebeck effect, the Schwinger mechanism plays a crucial role in photocurrent generation when graphene is laterally biased near the CNP.

Discussion

Nanoscale light-matter interactions offer a unique perspective for studying quantum electrodynamics on a chip. In this study, we have first revealed that the current-driven Cherenkov phonon emission induces an asymmetric plasmon damping effect in doped graphene. The nonequilibrium phonons also lead to unusual nano-photocurrent

responses, which exhibit reversed polarity compared to the bolometric photocurrent due to tip perturbation on phonon emission. Near the CNP, graphene exhibits enhanced photoconductivity due to Schwinger-type electron-hole pair generation, observable in nano-photocurrent signals across the sample. This effect is coupled with self-gating, which introduces an inhomogeneous electric field, crucial in shaping the local Schwinger photocurrent. By integrating infrared photons and electrical probes to the nanoscale, we have gained local insights into the interplay between drifting carriers, plasmons, phonons and photocurrent generation under high currents. Looking ahead, we anticipate that nano-infrared imaging methodology will greatly enhance our ability to explore intriguing physics in more current-driven nonequilibrium systems, such as in Moiré materials^{42,43}, Weyl semimetals⁴⁴, and other complex quantum materials.

Methods

Sample preparation

The device structure comprises an exfoliated monolayer graphene encapsulated by two hexagonal boron nitride layers with different thickness. The structure is assembled on a global Si or graphite gate at the bottom for tuning the graphene carrier density. The bottom boron nitride layer was ~40 nm for Si gate and 100 nm for graphite gate sample. The thin top boron nitride layer is around 2 nm, protecting graphene during fabrication and transparent enough for optical microscopy measurements. The stack was assembled from bottom to top by a PDMS (Polydimethylsiloxane) stamp coated with polypropylene carbonate film, flipped onto a silicon chip with 285 nm SiO₂ layer to minimize the polymer contaminations on its top surface. The chip was vacuum annealed at 360 Celsius degrees for 30 min to remove the polypropylene carbonate film beneath the heterostructure. We used electron beam lithography to define mask patterns and reactive-ion etching to shape the graphene to a ribbon geometry. Finally, metal film (2 nm Cr and 100 nm Au) was evaporated under high vacuum conditions (10⁻⁸ torr) to achieve the high-quality one-dimensional edge contacts.

Experimental setup

All the nano-infrared imaging experiments were conducted with a home-built cryogenic scanning nearfield microscope under ultra-high vacuum (<10⁻⁹ mbar). A quantum cascade laser from Daylight Solutions was used for exciting the plasmon polaritons and inducing photocurrent. The tapping AFM tip with PtSi coating was around 15 nm in diameter, which demodulated both scattering optical signals and photocurrent in nearfield. The plasmon polaritons were observed as fringes in both the nearfield optical scattering and bolometric photocurrent signals. These polaritons were launched by the gold electrodes and detected by the tip after propagating along the sample. The periods of the interference patterns matched full polariton wavelengths rather than half, indicating the propagating nature rather than standing waves. The SNOM modality was realized by the pseudo-heterodyne⁴⁵ method where scattered optical signals were demodulated by an AFM tip and a dithering reference mirror before being collected by a HgCdTe detector. The third order pseudo-heterodyne signals were then extracted with a Zurich HF2LI lock-in amplifier as output nearfield optical signals. The photocurrent was locally generated, demodulated by tip and measured from drain electrodes after the ground, amplified by a Femto DHPA-100 current amplifier, and locked to the tip tapping frequency by a Zurich MFLI lock-in amplifier. The second order demodulated photocurrent signals were used to isolate nearfield contribution. The DC current was sourced by a Keithley 2450 current source meter with values defined relative to the sample ground.

Data availability

Relevant data supporting the key findings of this study are available within the article and the Supplementary Information file. All raw data

generated during the current study are available from the corresponding authors upon request.

References

1. Oka, T. & Aoki, H. Photovoltaic Hall effect in graphene. *Phys. Rev. B* **79**, 081406 (2009).
2. McIver, J. W. et al. Light-induced anomalous Hall effect in graphene. *Nature Physics* **16**, 38–41 (2019).
3. Ni, G. X. et al. Ultrafast optical switching of infrared plasmon polaritons in high-mobility graphene. *Nature Photonics* **10**, 244–247 (2016).
4. Andersen, T. I. et al. Electron-phonon instability in graphene revealed by global and local noise probes. *Science* **364**, 154–157 (2019).
5. Greenaway, M. T. et al. Graphene's non-equilibrium fermions reveal Doppler-shifted magnetophonon resonances accompanied by Mach supersonic and Landau velocity effects. *Nat. Commun.* **12**, 6392 (2021).
6. Berdyugin, A. I. et al. Out-of-equilibrium criticalities in graphene superlattices. *Science* **375**, 430–433 (2022).
7. Schmitt, A. et al. Mesoscopic Klein-Schwinger effect in graphene. *Nat. Phys.* **19**, 830–835 (2023).
8. Tian, H. et al. Evidence for Dirac flat band superconductivity enabled by quantum geometry. *Nature* **614**, 440–444 (2023).
9. Schwinger, J. On Gauge Invariance and Vacuum Polarization. *Physical Review* **82**, 664 (1951).
10. Allor, D., Cohen, T. D. & McGady, D. A. Schwinger mechanism and graphene. *Phys. Rev. D* **78**, 096009 (2008).
11. Dóra, B. & Moessner, R. Nonlinear electric transport in graphene: Quantum quench dynamics and the Schwinger mechanism. *Phys. Rev. B* **81**, 165431 (2010).
12. Barajas-Aguilar, A. H. et al. Electrically driven amplification of terahertz acoustic waves in graphene. *Nat. Commun.* **15**, 2550 (2024).
13. Spector, H. N. Amplification of Acoustic Waves through Interaction with Conduction Electrons. *Physical Review* **127**, 1084 (1962).
14. Yamashita, J. & Nakamura, K. *Instability of the Electron-Phonon System in Strong Electric Fields. Progress of Theoretical Physics* **33**, 1022–1049 (1965).
15. Charles, K. *Introduction to Solid State Physics*, Chapter 6 and 14 (John Wiley & Sons, 2013).
16. Dong, Y. et al. Fizeau drag in graphene plasmonics. *Nature* **594**, 513–516 (2021).
17. Zhao, W. et al. Efficient Fizeau drag from Dirac electrons in monolayer graphene. *Nature* **594**, 517–521 (2021).
18. Kaminer, I. et al. Efficient plasmonic emission by the quantum Čerenkov effect from hot carriers in graphene. *Nat. Commun.* **7**, ncomms11880 (2016).
19. Wong, L. et al. Towards graphene plasmon-based free-electron infrared to X-ray sources. *Nature Photon.* **10**, 46–52 (2016).
20. Li, P. et al. Electroluminescence from graphene excited by electron tunneling. *Nanotechnology* **25**, 055206 (2014).
21. Kim, Y. et al. Bright visible light emission from graphene. *Nature Nanotech.* **10**, 676–681 (2015).
22. Woessner, A. et al. Near-field photocurrent nanoscopy on bare and encapsulated graphene. *Nat. Commun.* **7**, 10783 (2016).
23. Alonso-González, P. et al. Acoustic terahertz graphene plasmons revealed by photocurrent nanoscopy. *Nature Nanotech.* **12**, 31–35 (2017).
24. Ma, Q. et al. Photocurrent as a multiphysics diagnostic of quantum materials. *Nat. Rev. Phys.* **5**, 170–184 (2023).
25. Sunku, S. S. et al. Nano-photocurrent Mapping of Local Electronic Structure in Twisted Bilayer Graphene. *Nano Lett.* **20**, 2958–2964 (2020).

26. Song, J. C. W. & Levitov, L. S. Shockley-Ramo theorem and long-range photocurrent response in gapless materials. *Phys. Rev. B* **90**, 075415 (2014).
27. Shautsova, V. et al. Plasmon induced thermoelectric effect in graphene. *Nat. Commun.* **9**, 5190 (2018).
28. Gabor, N. M. et al. Hot carrier-assisted intrinsic photoresponse in graphene. *Science* **334**, 648–652 (2011).
29. Jago, R., Malic, E. & Wendler, F. Microscopic origin of the bolometric effect in graphene. *Phys. Rev. B* **99**, 035419 (2019).
30. Freitag, M. et al. Photoconductivity of biased graphene. *Nature Photon.* **7**, 53–59 (2013).
31. Ni, G. X. et al. Fundamental limits to graphene plasmonics. *Nature* **557**, 530–533 (2018).
32. Grosse, K. et al. Nanoscale Joule heating. *Peltier cooling and current crowding at graphene–metal contacts*. *Nature Nanotech* **6**, 287–290 (2011).
33. Vera-Marun, I. et al. Direct electronic measurement of Peltier cooling and heating in graphene. *Nat. Commun.* **7**, 11525 (2016).
34. Zarembo, K. Joule–Thomson Cooling in Graphene. *JETP Lett.* **111**, 157–161 (2020).
35. Sabbaghi, M., Stauber, T., Lee, H. W., Gomez-Diaz, J. S. & Hanson, G. W. In-plane optical phonon modes of current-carrying graphene. *Phys. Rev. B* **105**, 235405 (2022).
36. Yang, W. et al. A graphene Zener–Klein transistor cooled by a hyperbolic substrate. *Nature Nanotech.* **13**, 47–52 (2018).
37. Guo, Q. et al. Hyperbolic phonon-polariton electroluminescence in 2D heterostructures. *Nature* **639**, 915–921 (2025).
38. Principi, A. et al. Plasmon losses due to electron-phonon scattering: The case of graphene encapsulated in hexagonal boron nitride. *Phys. Rev. B* **90**, 165408 (2014).
39. Sun, Z., Basov, D. N. & Fogler, M. M. Third-order optical conductivity of an electron fluid. *Phys. Rev. B* **97**, 075432 (2018).
40. Ho, D. Y. H., Yudhistira, I., Chakraborty, N. & Adam, S. Theoretical determination of hydrodynamic window in monolayer and bilayer graphene from scattering rates. *Phys. Rev. B* **97**, 121404 (2018).
41. Wang, F. et al. Gate-Variable Optical Transitions in Graphene. *Science* **320**, 206–209 (2008).
42. Sunku, S. S. et al. Hyperbolic enhancement of photocurrent patterns in minimally twisted bilayer graphene. *Nat. Commun.* **12**, 1641 (2021).
43. Hesp, N. C. H. et al. Nano-imaging photoresponse in a moiré unit cell of minimally twisted bilayer graphene. *Nat. Commun.* **12**, 1640 (2021).
44. Shao, Y. et al. Nonlinear nanoelectrodynamics of a Weyl metal. *Proc. Natl. Acad. Sci. USA* **118**, e2116366118 (2021).
45. Ocelic, N., Huber, A. & Hillenbrand, R. Pseudoheterodyne detection for background-free near-field spectroscopy. *Appl. Phys. Lett.* **89**, 101124 (2006).

Acknowledgements

This work was mainly supported by Programmable Quantum Materials, an Energy Frontier Research Center funded by the U.S. Department of Energy (DOE), Office of Science, Basic Energy Sciences (BES), under award no. DE-SC0019443. D.N.B. is a Moore Investigator in Quantum Materials EPIQS no. 9455. D.A.B. is supported by the Ministry of

Education, Singapore, under its Academic Research Fund Tier 2 (T2EP50123-0020). Work at the P.J.H. lab was primarily supported by the Air Force Office of Scientific Research (Grant FA9550-21-1-0319), the Massachusetts Institute of Technology/Microsystems Technology Laboratories Samsung Semiconductor Research Fund, by the Gordon and Betty Moore Foundation Emergent Phenomena in Quantum Systems Initiative (Grant GBMF9463) and by the Fundación Ramon Areces.

Author contributions

Y.D. conducted the experiments and analysis using devices fabricated by I.Y.P., D.A.B., and D.S., under the supervision of P.J.H., P.K., C.R.D., and D.N.B. Z.S., T.I.A., and A.R. contributed to the theoretical frameworks under the guidance of A.J.M. and M.M.F. L.X., Y.S., S.Z., and S.L. contributed to the experiments. Y.D. D.A.B. and D.N.B. led the discussions with participation from all co-authors.

Competing interests

The authors declare no competing interests.

Additional information

Supplementary information The online version contains supplementary material available at <https://doi.org/10.1038/s41467-025-58953-6>.

Correspondence and requests for materials should be addressed to Y. Dong, D. A. Bandurin or D. N. Basov.

Peer review information *Nature Communications* thanks Dmitry Turchinovich, who co-reviewed with Hassan Hafez and the other, anonymous, reviewers for their contribution to the peer review of this work. A peer review file is available.

Reprints and permissions information is available at <http://www.nature.com/reprints>

Publisher's note Springer Nature remains neutral with regard to jurisdictional claims in published maps and institutional affiliations.

Open Access This article is licensed under a Creative Commons Attribution-NonCommercial-NoDerivatives 4.0 International License, which permits any non-commercial use, sharing, distribution and reproduction in any medium or format, as long as you give appropriate credit to the original author(s) and the source, provide a link to the Creative Commons licence, and indicate if you modified the licensed material. You do not have permission under this licence to share adapted material derived from this article or parts of it. The images or other third party material in this article are included in the article's Creative Commons licence, unless indicated otherwise in a credit line to the material. If material is not included in the article's Creative Commons licence and your intended use is not permitted by statutory regulation or exceeds the permitted use, you will need to obtain permission directly from the copyright holder. To view a copy of this licence, visit <http://creativecommons.org/licenses/by-nc-nd/4.0/>.

© The Author(s) 2025